

PL-TR-96-1052

PL-TR-
96-1052

IMPROVED, HIGH POWER, EYE SAFE, SOLID STATE LASER

R.A. Stolzenberger

**Crystal Associates, Inc.
15 Industrial Park
Waldwick, NJ 07463**

March 1996

Final Report

APPROVED FOR PUBLIC RELEASE; DISTRIBUTION IS UNLIMITED.

19960508 236

DTIC QUALITY INSPECTED 3



**PHILLIPS LABORATORY
Lasers and Imaging Directorate
AIR FORCE MATERIEL COMMAND
KIRTLAND AIR FORCE BASE, NM 87117-5776**

Using Government drawings, specifications, or other data included in this document for any purpose other than Government procurement does not in any way obligate the U.S. Government. The fact that the Government formulated or supplied the drawings, specifications, or other data, does not license the holder or any other person or corporation; or convey any rights or permission to manufacture, use, or sell any patented invention that may relate to them.

This report has been reviewed by the Public Affairs Office and is releasable to the National Technical Information Service (NTIS). At NTIS, it will be available to the general public, including foreign nationals.

If you change your address, wish to be removed from this mailing list, or your organization no longer employs the addressee, please notify PL/LIDA, 3550 Aberdeen Ave SE, Kirtland AFB, NM 87117-5776.

Do not return copies of this report unless contractual obligations or notice on a specific document requires its return.

This report has been approved for publication.



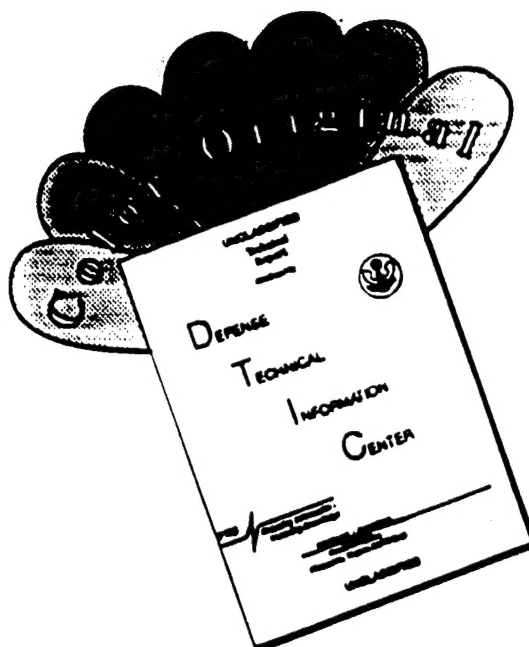
PETER S. DURKIN
Project Manager


NICHOLAS R. PCHELKIN, GM-15
Chief, LIDA

FOR THE COMMANDER


ROBERT A. DURYEA, Col, USAF
Director, Lasers and Imaging Directorate

DISCLAIMER NOTICE



**THIS DOCUMENT IS BEST
QUALITY AVAILABLE. THE COPY
FURNISHED TO DTIC CONTAINED
A SIGNIFICANT NUMBER OF
COLOR PAGES WHICH DO NOT
REPRODUCE LEGIBLY ON BLACK
AND WHITE MICROFICHE.**

DRAFT SF 298

1. Report Date (dd-mm-yy) March 1996	2. Report Type Final Report	3. Dates covered (from... to) 24 Aug 95 - 24 Sep 95		
4. Title & subtitle IMPROVED, HIGH POWER, EYE SAFE, SOLID STATE LASER		5a. Contract or Grant # F29601-95-C-0118		
		5b. Program Element # 65502F		
6. Author(s) Richard A. Stolzenberger		5c. Project # 3005		
		5d. Task # C0		
		5e. Work Unit # LM		
7. Performing Organization Name & Address Crystal Associates Inc. 15 Industrial Park Waldwick, NJ 07463		8. Performing Organization Report #		
9. Sponsoring/Monitoring Agency Name & Address Phillips Laboratory 3550 Aberdeen Avenue, SE Kirtland AFB, NM 87117-5776		10. Monitor Acronym LIDA		
		11. Monitor Report # PL-TR-96-1052		
12. Distribution/Availability Statement Approved for Public Release; Distribution is Unlimited				
13. Supplementary Notes				
14. Abstract The Phase I SBIR technical results demonstrate the feasibility of a solid-state Raman shifter to generate 1.56 micron light. The 1.56 micron laser source was based on a compact, Nd:YAG-pumped, intracavity Barium Nitrate, solid-state Raman shifter (SSRS). The experiment demonstrated diffraction limited, 1.56 micron output at greater than 250 mJ/pulse, with an optical-to-optical conversion efficiency of 60%. Some nice features of this novel technique were a very large aperture (7.5 mm, used for maximum power extraction) and conversion of the highly multimode pump beam to a diffraction limited, single transverse mode output via nonlinear Raman clean-up. Optical damage was avoided through the optical limiting properties of an intracavity nonlinear element. Extremely high conversion efficiency was achieved, and the measured Raman gain in Barium Nitrate was a record 11 cm/GW @ 1.064 micron. This Phase I effort provided a laboratory demonstration of the SSRS system capabilities, including pulse repetition rate scaling.				
15. Subject Terms Eye-safe, Raman shifting, Solid-state lasers, Barium Nitrate				
Security Classification of				
16. Report Unclassified	17. Abstract Unclassified	18. This Page Unclassified	19. Limitation of Abstract Unlimited	20. # of Pages 46
21. Responsible Person (Name and Telephone #) Maj Peter S. Durkin 505-846-5913				

PREFACE

This document constitutes Data item No. 0002, the Final Technical Report by Crystal Associates, Inc., Waldwick, NJ as required by U.S. Department of Defense Contract No. F29601-95-C-0118 "Improved, High Power, Eye Safe, Solid State Laser". The program reported herein was awarded under SBIR Topic Number AF95-106 and conducted during the 24 month period beginning March 24, 1995 and ending October 15, 1995. Computer modeling and prototype characterization was carried out by Lite Cycles, Inc. in Tuscon, AZ.

TABLE OF CONTENTS

1. INTRODUCTION	1
2. MATERIALS PREPARATION	2
2.1. Growth	2
2.2. Ba(NO ₃) ₂ crystal fabrication and polishing	2
2.3. Antireflective coating	3
3. CHARACTERIZATION	3
3.1. Optical transmission	3
3.2. Raman Stokes shift	4
3.3. Optical damage threshold	4
3.4. External resonator operation	5
4. PERFORMANCE MODELING AND DESIGN	5
4.1. Lasica: Laser Design Code	6
4.2. Astigmatism Correction	7
4.2.1. Astigmatically Compensated Resonator Design: Example	8
4.2.2. Mode-matching Techniques in Intracavity Raman Lasers	14
4.3. Power Limiting Thermal Effects	17
4.4. Cavity Mode Build-up Dynamics	20
4.5. Intracavity Raman Beam Cleanup	22
4.5.1. Computer Modeling of Intracavity Raman Beam Cleanup	24
4.6. Resonator Dynamics	26
4.7. Pump Characterization	27
4.8. Raman Characteristics	28
5. COMMERCIAL ANALYSIS	30
6. RESULTS AND CONCLUSIONS	32

LIST OF FIGURES

FIGURE 1: Transmission vs. Wavelength for 3mm Pathlength Ba(NO ₃) ₂ Crystal	4
FIGURE 2: Ba(NO ₃) ₂ Optical Damage Threshold	5
FIGURE 3: Zig-Zag Slab Geometry	8
FIGURE 4: High Average Power Intracavity Raman Laser	8
FIGURE 5: Astigmatically Compensated Laser Cavity Example	9
FIGURE 6: Unfolded Resonators: (A) Pump Laser Cavity, and (B) Raman Laser Cavity	10
FIGURE 7: Astigmatically Compensated Raman Laser Tangential (Blue) and Sagittal (Red) Eigenmodes	12
FIGURE 8: Tangential (Blue) and Sagittal (Red) Eigenmodes of the Pump Laser Cavity when the Raman Laser Eigenmodes are Astigmatically Compensated.	13
FIGURE 9: Overlapping Stability Curves for Raman Cavity (Upper two curves) and Pump Laser Cavity (Lower two curves)	14
FIGURE 10: Mode-matched Coupled Pump and Raman Laser Eigenmodes	16
FIGURE 11: Dynamic Cavity Stability of the Example High Average Power Laser Cavity as a Function of the Thermal Focal Length of the Thermally Loaded Nd:YAG Laser Rod (In mm)	18
FIGURE 12: Eigenmodes Variation with Thermal Focal Length of Laser Rod	19
FIGURE 13: Transient Sagittal Mode Evolution of the Example Raman Laser	22
FIGURE 14: Example Travelling Wave Resonator used to Demonstrate Intracavity Raman Beam Cleanup	25
FIGURE 15: Intracavity Beam Cleanup. (A) Multimode Pump Beam Profile (1.338μm) and (B) Single Mode, Diffraction Limited Stokes Beam Profile (1.556μm)	25
FIGURE 16: Pump (Blue) and First Stokes (Red) Transverse Field Distributions	26
FIGURE 17: Pulse Characteristics for 2.5 Watt Average Power Diode Pumped Slab	28

FIGURE 18: Raman Cavity Output Coupling and Peak Power Levels	29
FIGURE 19: Optical Layout of the Intracavity SSRS and Pump Laser	33
FIGURE 20: (A) Modeling of the Pump Depletion and Raman Emmision (B) Oscillascope Trace of the Temporal Profile of Pump and Raman Emission	34

1. 1. INTRODUCTION

There is current need for compact, all solid-state, efficient, robust eye-safe lasers capable of 3 to 100 W of diffraction limited, 1.56 μm radiation, Q-switched at 50 Hz to 10 kHz. The current state-of-the-art 1.56 μm laser systems utilize high pressure, external cavity D₂ Raman shifters to convert the output from 1.064 μm Nd:YAG lasers. These sources have difficulty scaling to average powers greater than 10 W, are limited to ~50% optical-to-optical conversion efficiency, and output marginal beam quality. A potential all solid-state candidate for a power scaled, 1.56 μm laser is the Nd:YAG pumped Optical Parametric Oscillator (OPO). However, recent attempts to power scale OPOs have met with little success. These failures are due mainly to: (1) inadequate transmission in the converting medium which causes thermal dephasing at high average powers and (2) optical damage in the OPO optics resulting from either the high fluence (~50 J/cm²) pump radiation or the 3.35 μm idler absorption. OPOs that have been successfully scaled to ~200 mJ/pulse have utilized large pump diameters (~7 mm) in small OPO resonators (~3 cm) which yield many times diffraction limited output beams which are not suitable for long-range remote sensing sources.

The results of this Phase I effort along with recently published work^{1,2,3} indicate a much more elegant, all solid-state technique, which utilizes a proven power

¹ J.T. Murray, R.C. Powell, N. Peyghambarian, D.D. Smith, W. Austin and R. Stolzenberger," Stimulated Raman Scattering and Intracavity Beam Clean-up," Proc. Nonlinear Optics '94 Conference, Postdeadline, July, 1994, Kona Hawaii.

² J.T. Murray, R.C. Powell, N. Peyghambarian, D.D. Smith, W. Austin and R. Stolzenberger," Generation of 1.5 μm Radiation Through Intracavity Solid-State Raman Shifting in Ba(NO₃)₂ Nonlinear Crystals," Opt. Lett. 20, 1017 (1995)

³ J.T. Murray, R.C. Powell, N. Peyghambarian, D.D. Smith and W. Austin," Eye-Safe Solid-State Intracavity Raman Laser," Proc. Advanced Solid State Lasers Conference '95, Memphis, TN

scaleable design. The 1.56 μm laser source is based on a compact Nd:YAG pumped, intracavity Ba(NO₃)₂ solid-state Raman shifter (SSRS). We have demonstrated diffraction limited, 1.56 μm output at greater than 250 mJ/pulse, with an optical-to-optical conversion efficiency of 60%. Several features contribute to the appeal of this novel technique. A very large aperture (7.5 mm) is utilized for maximum power extraction. The highly multimode pump beam is converted to a diffraction limited, single transverse mode 1.56 μm output via nonlinear Raman clean-up. Optical damage is avoided through the optical limiting properties of an intracavity nonlinear element. Extremely high conversion efficiency is achieved since the quantum efficiency is 85% and the Raman gain in Ba(NO₃)₂ is a record 11 cm/GW @ 1.064 μm (the gain of D₂ is 1.5 cm/GW).

The Phase I effort accomplished the repetition rate scaling for the SSRS technology and provided a laboratory demonstration of the SSRS system capabilities. This work has demonstrated the feasibility of a field ready, compact, rugged, diode pumped, 3 Watt eye-safe laser source.

2. MATERIALS PREPARATION

2.1. *Growth*

Low temperature aqueous solution growth of Ba(NO₃)₂ was successfully scaled to yield large high quality single crystals boules (free of cracks, voids, veils, inclusions etc.).

2.2. *Ba(NO₃)₂ crystal fabrication and polishing.*

Single crystal Raman conversion elements were fabricated from the grown boules with 20,50,80, and 100 mm nominal length. The nominal aperture in each case was 10 x 10 mm². Elements were fabricated with flat and Brewster

angle faces. Continually evolving polishing techniques have produced crystals sufficient for the characterization performed in the Phase I effort. However, further improvements in polishing are necessary to reduce scratch and dig in order to decrease the insertion losses for the actual resonator applications. Current scratch/dig figures of merit are 60/40. Further development in polishing technique is expected to yield scratch/dig figures of 20/10.

2.3. *Anti reflection coating*

Sol-gel coating technology employed in coating KDP (also hygroscopic) was employed in the Phase I effort to AR coat Ba(NO₃)₂. While this sol-gel coating was successful in providing anti-reflecting surfaces, it does not provide protection from damage due to atmospheric moisture. In addition, this coating is soft and easily damaged if touched. Alternative AR schemes (other coatings or sealed cells with AR coatings) will be evaluated during the Phase II investigation and the most appropriate will be selected to be included in the final 1.56 μm laser source demonstrated at the end of that effort.

3. CHARACTERIZATION

3.1. *Optical transmission*

The transmission of a 3 mm thick Ba(NO₃)₂ crystal was measured using a Perkin Elmer 330 Spectrophotometer. The transmission vs. wavelength is shown in Figure 1.

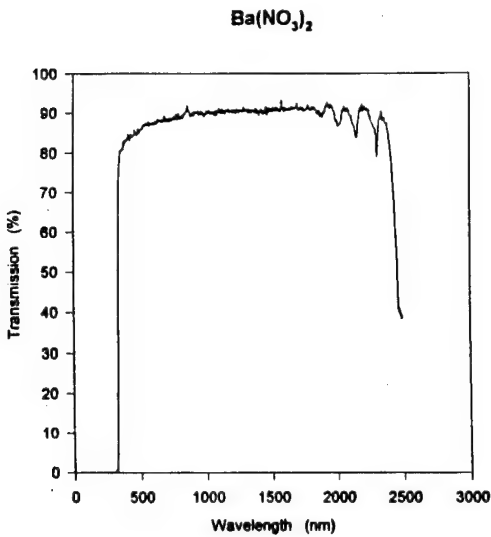


Figure 1: Transmission vs. wavelength for 3 mm pathlength $\text{Ba}(\text{NO}_3)_2$ crystal.

3.2. Raman Stokes shift

The wavelength shift of the 1064 nm line of a J-K HY-750 q-switched Nd:YAG laser was measured after Stokes shifting with a 50 mm long $\text{Ba}(\text{NO}_3)_2$ crystal. A 1/4 meter Photon Technology International spectrometer was used to determine the wavelength. The Raman shift was found to be $1198 \pm 3 \text{ nm}$ as expected. This confirms the published Raman Stokes Shift of about 1047 cm^{-1} .

3.3. Optical damage threshold

The damage threshold of a $\text{Ba}(\text{NO}_3)_2$ sample crystal was measured by Dale A. Richter of Science Applications International Corp. using a q-switched, frequency doubled YAG laser operating at 532 nm. The details of the measurement are given in Figure 2. The material was found to damage at a fluence of approximately 9 J/cm^2 .

wavelength	532 nm
incident angle	2°
beam profile	near gaussian
pulse length	7 ns

Energy (J)	Beam Rad (cm)	Gaussian Fit (%)	Fluence (J/cm ²)	Damage (yes/no)
0.025	0.047	0.9	6.43	no
0.03	0.047	0.9	7.71	no
0.045	0.047	0.9	11.57	yes
0.085	0.056	0.88	15.18	yes

Figure 2: Ba(NO₃)₂ Optical damage threshold

3.4. External resonator operation

Preliminary experiments in an external resonator demonstrated stimulated Stokes shifted radiation with first Stokes efficiency of approximately 30% with approximately 2.0 mrad beam divergence.

4. PERFORMANCE MODELING AND DESIGN

Several aspects of intracavity high-average power Raman lasers have not been fully developed until recently. The most economical high power Raman laser designs utilize coupled cavity power oscillator configurations. In these configurations nearly all pump photons are converted to the first Stokes photons, giving near quantum limited performance for the system. When properly

optimized, these cavities can output high brightness, near diffraction limited Stokes radiation from highly multimode intracavity pumping fields. As a result, the overall efficiency (from inverted ions to first Stokes photons) can be very high-leading to wall-plug efficiencies of nearly 8% for diode pumped systems.

Here we will present the main design considerations of high average-power intracavity Raman lasers. The topics discussed are astigmatism correction, coupled cavity mode-matching, dynamic cavity stability and cavity buildup dynamics. For the sake of brevity, we will discuss the main high power design considerations in the context of one representative system. Although the overall appearance of the system may change, the concepts discussed remain valid for other systems.

The preliminary design for a solid state Raman converted 25 mJ per pulse 100Hz rep rate eye safe laser transmitter operating at 1.56 μm is presented in this section. Models for power scaling solid state laser systems include resonator thermal effects and intracavity Raman laser dynamics. These models were developed for a 2.5 watt average power output system.

This preliminary modeling effort was based on system requirements and was accomplished for the Phase I contract effort and to estimate the detailed tasks and times for the eye safe transmitter project outlined in the Phase II proposal.

4.1. Lasica: Laser Design Code

A laser design software package (*Lasica*) was written in *Mathematica* to aid in the design of these complex coupled cavity Raman laser resonators and other nonlinear optical systems: such as Raman image amplifiers, optical parametric oscillators and frequency doubling systems. *Lasica* is designed to accept a

simple list of optical elements and translations to invoke any level of modeling, making the code efficient and easy to use.

4.2. Astigmatism Correction

The geometry of the laser host material and Raman crystal material govern the ultimate power scalability of high-average-power Raman oscillators. Thermal loading of these materials is unavoidable due to intrinsic quantum defects in both the laser and Raman processes. As will be discussed in detail in Sec. 5.1.3, the deleterious effects of thermally induced focusing and birefringence are canceled to first order when zig-zag slab geometries are employed (see Figure 3). Therefore, thermally stationary, high-average-power intracavity Raman oscillators should employ zig-zag slab laser and Raman medium (see Figure 4). However, a degree of aberration compensation is still necessary. Because Raman conversion is a nonlinear process, efficient conversion is only achieved in tightly focused resonator configurations. As a result, a large astigmatism is imparted on the oscillating beams due to the varying path lengths experienced between the focused tangential and sagittal components in the zig-zag slab. In most cases the astigmatism incurred is large enough to render the cavity unstable. A technique must therefore be employed to compensate for this astigmatism. The following section will address astigmatism compensation techniques in the context of a particular experimental resonator design. *Lasica* has been equipped with generalized astigmatism compensation algorithms.

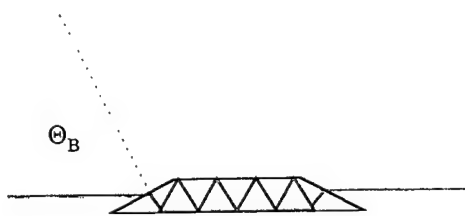


Figure 3: Zig-zag slab geometry. Optical beams, polarized in the plane of incidence, enter and exit the trapezoidal slab at Brewster's angle, θ_B . These beams are trapped by total internal reflection (TIR) within the medium.

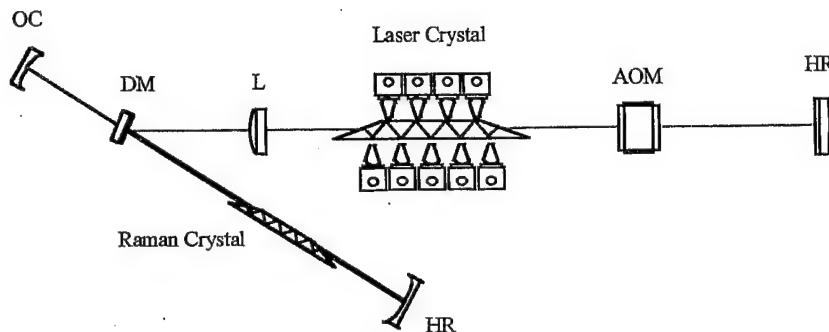


Figure 4: High-average-power intracavity Raman laser. Thermally stationary Raman oscillators employ zig-zag slab geometries for both the laser and Raman crystals to mitigate first order thermally induced lensing and birefringence. HR, high reflector, OC, output coupler, AOM, acoustooptic modulator, L, lens.

Figure 5 shows the cavity layout of a particular intracavity coupled cavity Raman laser and Figure 6 displays the corresponding unfolded pump and Raman cavities for this system.

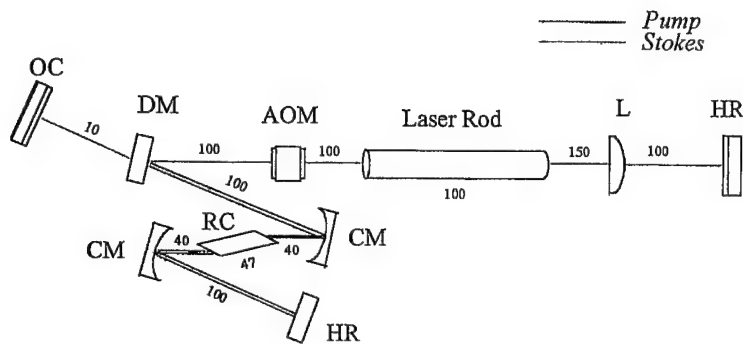


Figure 5: Astigmatically compensated laser cavity example. The optical elements in the cavity are: HR, high reflector; OC, output coupler; CM, 100 mm roc curved mirror; DM, dichroic mirror; L, 500 mm focal length thin lens; AOM, acoustooptic modulator; and RC, 10 x 10 x 47 mm³ Brewster cut Raman crystal. All distances reported are in mm.

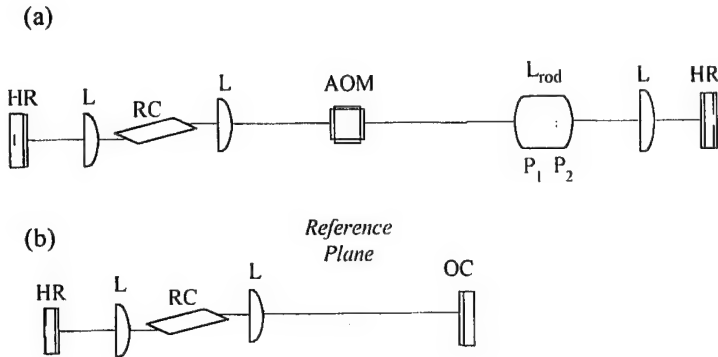


Figure 6: Unfolded resonators: (a) Pump laser cavity, and (b) Raman laser cavity. All curved mirrors CM, are replaced by lenses L, in the unfolded resonators. The value of the focal length of each lens are dissimilar in the tangential and sagittal planes due to the astigmatism induced by the tiled curved mirrors. The thermally loaded laser rod has been replaced by a thick-lens with equivalent effective focal length L_{rod} and principle planes P_1 and P_2 . The reference plane in the Raman cavity is the plane in which the astigmatism is canceled. The stokes eigenmode will be stigmatic between the lens L, which is the unfolded version of the curved mirror CM, and the output coupler OC.

In the unfolded resonators the curved mirrors are replaced with equivalent lenses with nominal focal lengths equal to half the mirror radius of curvature (roc). However, because the incident beams enter the curved mirrors at an angle, the effective focal length of the equivalent lenses in the tangential and sagittal planes will be dissimilar⁴, inducing an astigmatism. Fortunately, the astigmatism induced by the tilted curved mirrors is of opposite sign to that incurred in the Raman crystal. The overall astigmatism can, therefore, be canceled in one branch of the resonator by selecting the appropriate tilt angle on the mirrors.

The particular cavity design described in this example was implemented for early high repetition rate (1 to 10 kHz) eye-safe laser experiments. For this resonator, the pump and Raman resonator layouts are in the form of standard standing-wave z-cavity and linear cavities, respectively. A dichroic mirror (DM), which is highly reflective (HR) at 1.338 μm and highly transmitting (HT) at the first Stokes wavelength of 1.556 μm , was used to couple the pump and Raman cavities. All other mirrors in the pump laser cavity were HR's at both pump and first Stokes wavelengths. The Raman cavity shared the folded end of the pump laser cavity.

The laser medium consisted of a 6 x 100 mm Nd:YLF rod, which was pumped by a cw arclamp. The average power delivered to the arclamp is nominally 3 kW. At this power level the laser rod becomes thermally loaded, inducing an extended thermal focal length. It is well known that the optical power associated with the thermal lensing can be treated by replacing the extended thermal lens with a thick-lens having an input power dependent effective focal length and principle plane separation⁶.

A novel astigmatism correction technique was developed and included in *Lasica*. In our technique a reference plane is selected where the astigmatism is to be canceled. This plane can be arbitrarily set anywhere within the cavity. In this example the reference plane is selected to lie in-between the dichroic mirror (DM) and the Raman laser output coupler (OC). This plane is chosen to assure that the Raman output be stigmatic, i.e. circularized output beam. An astigmatism will remain in the Raman crystal because the resonator can only be stigmatic in one arm. The overall performance of the Raman laser is not compromised.

Utilizing *Lasica* to solve for the curved mirror tilt angle in this example, we find $\theta_{\text{tilt}} = 26.8^\circ$. This routine is completely general in that any laser system with

astigmatic elements can be rendered stigmatic by *Lasica* in one arm of the resonator. Figure 7 shows the resulting beam radius of the lowest order eigenmode for the astigmatically compensated Raman cavity in this example. The tangential and sagittal beam waists are equivalent throughout the branch containing the Raman output coupler (between M1 and MXI in the figure).

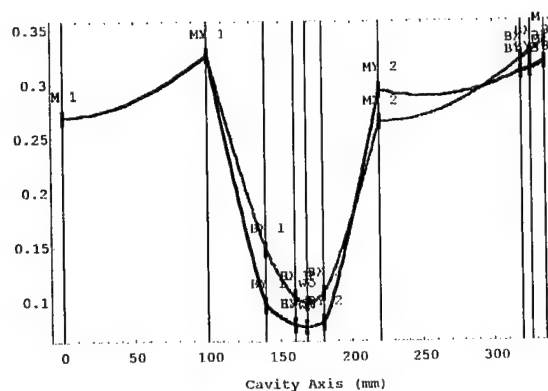


Figure 7: Astigmatically compensated Raman laser tangential (blue) and sagittal (red) eigenmodes. The vertical axis is the transverse beam radius half-width (in mm), and the horizontal axis, the cavity dimension (in mm). Vertical lines mark the position of optical elements.

Figure 8 displays the lowest order eigenmode beam radius of the pump cavity when $\theta_{\text{tilt}} = 26.8^\circ$ is used for the curved mirror tilt angle. Here it is evident that nowhere in the pump cavity is the beam stigmatic. This is due to the difference in wavelength between the pump and Stokes beams, which translates into a difference in complex beam parameters q .

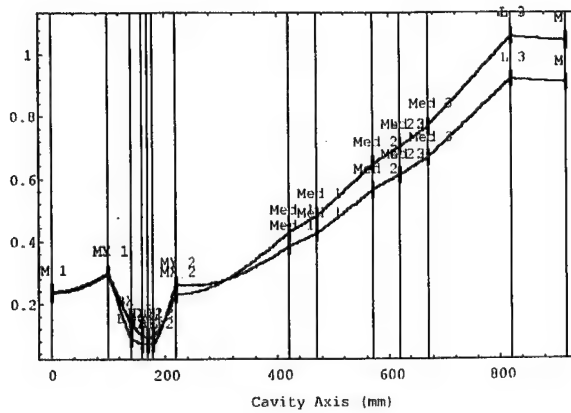


Figure 8: Tangential (blue) and sagittal (red) eigenmodes of the pump laser cavity when the Raman laser eigenmodes are astigmatically compensated. The vertical axis is the transverse beam half-width (in mm), and the horizontal axis, the cavity dimension (in mm).

Cavities with both large and small eigenmode beam diameters tend to be very sensitive to certain cavity parameters. In the cavity discussed here the stability is most sensitive to the relative crystal-mirror separation. This parameter effectively changes the focusing characteristics of the X1 telescope defined by the two 100 mm radius of curvature tilted mirrors. *Lasica* can be utilized to find the stability ranges and tolerances of cavity variables such as the telescope defocusing parameters or thermally loaded rod focal length. Coupled cavity designs, such as the design considered in this example, can vastly limit the range in parameter-space available to a geometrically stable resonator. In the example presented here the challenge is to find a crystal-mirror separation χ , which will render both the sagittal and tangential eigenmodes of both the pump and Raman cavities stable. In effect, the stability condition must be simultaneously satisfied by all four resonators for a particular value of the free

parameter χ . As is shown in Figure 9, it is not always possible to overlap the stability regions of all four cavities. In the case of Figure 9, χ represents the telescope defocusing parameter (i.e. the curved mirror crystal separation). As is shown, no values of χ simultaneously yield stability in all four resonators described in Figure 5. It is shown that for $\chi \approx 75$ mm, the sagittal eigenmode of the pump laser cavity and the tangential eigenmode of the Raman laser cavity are both unstable, and nowhere else do they overlap. To achieve the simultaneous stability condition, parameters, such as the rod focal length, can be varied along with χ .

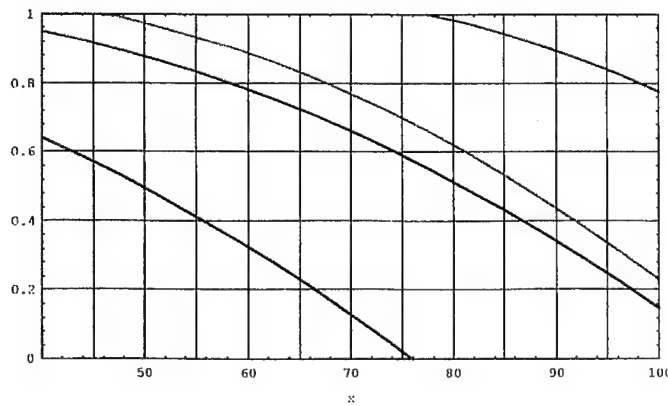


Figure 9: Overlapping stability curves for Raman cavity (upper two curves) and pump laser cavity (lower two curves). The sagittal (red) and tangential (blue) mode stabilities are shown for both cavities. The parameter χ in this example is the telescope defocusing parameter.

4.2.2. Mode-matching Techniques in Intracavity Raman Lasers.

Quantum limited optical-to-optical conversion efficiencies can only be achieved when the effective pump and Raman spatial modes are overlapped. When the pump laser cavity is designed to operate in a single spatial mode (which can be

accomplished by spatial filtering with a limiting intracavity aperture), the optimum conversion efficiency is achieved when the spatial mode of the pump exactly overlaps the lowest order eigenmode of the Raman cavity within the Raman medium. When this condition is satisfied the cavities are said to be "mode-matched".

In the case of the intracavity Raman laser discussed in the previous section, mode-matching can be achieved by varying either (or both) the radius of curvature (roc) of the Raman cavity output coupler (OC) or the distance between the OC and the dichroic mirror (DM). For the case discussed here, a $\text{roc of } \infty$ was selected and the mirror spacing between the OC and DM was varied.

Figure 10 below shows the overlapped cavity eigenmodes of both the pump and Raman cavities when the mode-matching routine is performed. Only a portion of the pump laser eigenmode is displayed in the figure to better show the region of overlap. Lasica has been programmed with a mode-matching algorithm to automate this procedure for arbitrary cavity designs.

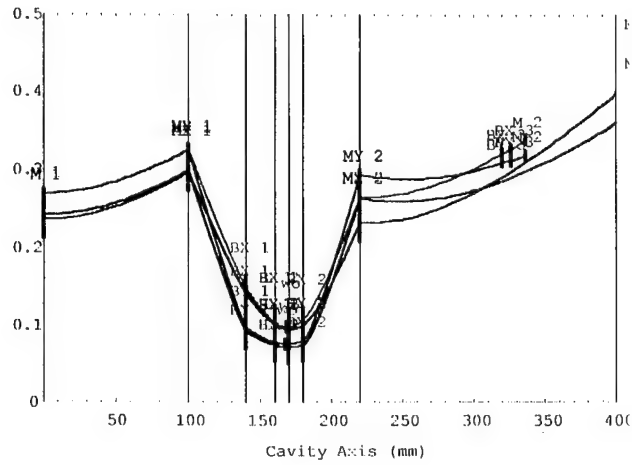


Figure 10: Mode-matched coupled pump and Raman laser eigenmodes. The pump cavity sagittal (red) and tangential (blue) eigenmodes are shown along with the Raman cavity sagittal (orange) and tangential (aqua) eigenmodes. Mode-matching was achieved by varying the dichroic mirror (B2) - output coupler (M2) separation. Only the portion of the pump laser eigenmode is shown to better show the eigenmode overlap. The vertical axis in the eigenmode beam transverse beam radius (in mm) and the horizontal axis is the cavity axis (in mm). All optical components are shared by both pump and Raman lasers accept the Raman output coupler (M2).

Contrary to other nonlinear frequency conversion processes, in the case of Raman frequency conversion, the stimulated Stokes radiation is driven by a nonlinear polarization field that depends on the irradiance distribution of the pumping field. Hence, no phase information in the pumping field is transferred to the Stokes field. Rather, the phase of the seeding Stokes field is replicated in the stimulated Stokes field. In view of this phenomena, the mode-matching criteria for Raman lasers can be relaxed to include the case where the single mode Stokes field is matched to the multimode beam diameter of the pump field. As will be discussed in more detail in Sec. 5.1.5, highly multimode intracavity pump radiation can be converted, through the process of Raman beam cleanup, to a single order intracavity Stokes spatial mode. As a result, the most efficient

use of the pump radiation is accomplished when the multimode pump beam diameter is matched to the single spatial mode Stokes beam diameter in the Raman crystal. Because multimode lasers can be designed to have access to nearly all the inverted population in the laser medium, the Stokes photon per inversion center ratio can be much larger in the case of multimode pump operation, hence, increasing the overall efficiency and brightness of the laser source. Therefore, the combination of a relaxed mode-matching condition and Raman beam cleanup phenomena leads to a very profound increase in the overall efficiency and brightness potential of Raman lasers.

Detailed spatial mode evolution modeling must be implemented to effectively predict the mode-matching condition of a single mode Stokes cavity to a multimode pump cavity. These calculations can be performed by utilizing the diffraction-propagation, laser and Raman gain modeling routines available in Lasica. These routines utilize the same resonator information required to obtain the solutions to the first order designs, and are therefore easily involved.

4.3. Power Limiting Thermal Effects

Thermal loading effects of intracavity optical elements can severely limit a lasers average-power capability. Under strong-pumping operating conditions laser host and Raman medium can exhibit optical distortions which include thermal focusing, stress induced biaxial focusing, and stress induced birefringence⁶. Thermal lensing not only leads to input power cavity instabilities but also to loss, which is caused by the asymmetry of the induced lens as will be discussed. In applications where the polarization of the pumping laser is important (e.g. electrooptic Q-switching, birefringent phase-matched nonlinear conversion, etc.),

thermally induced birefringence restricts the laser output power to a level well below the average power set by biaxial focusing and stress fracture.

Because the rods thermal focal length depends of the average input power to the lamps the cavity eigenmode will be dynamically dependent on the input power. Hence, the input power dynamically affects both the cavity stability and eigenmode structure. Figure 11 below shows the dynamic cavity stability as a function of rod focal length for a laser similar to the one shown in Figure 5. In this example the laser rod host material is Nd:YAG instead of Nd:YLF, which was used earlier. Also the lens has been removed between the laser rod and the cavity end mirror.

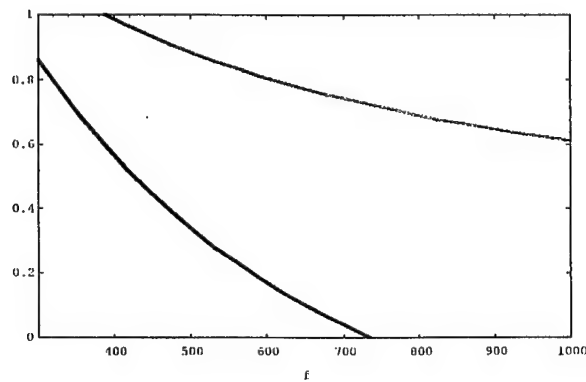


Figure 11: Dynamic cavity stability of the example high-average-power laser cavity as a function of the thermal focal length of the thermally loaded Nd:YAG laser rod (in mm). The functional dependence of the sagittal (red) and tangential (blue) dynamic stability are dissimilar as shown here.

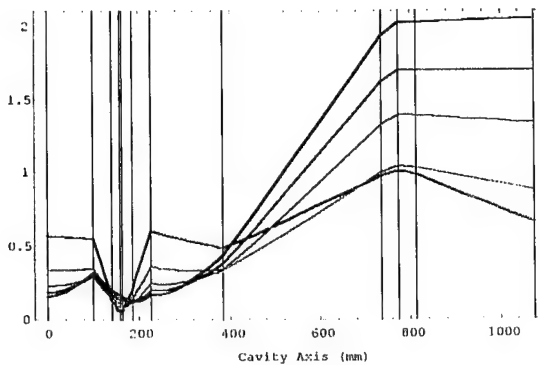


FIGURE 12: Eigenmode variation with thermal focal length of laser rod. Here it is shown how the sagittal eigenmode migrate as the power delivered to the laser medium increases and, hence, the thermally induced effective rod focal length decreases. The effective rod focal length decreases from 650nm (blue) to 450nm (red) as the input power varies from 3kW to 5kW, respectively. The vertical axis is the beam half-width (in mm) and the horizontal, the cavity axis (in mm). Vertical line mark the various intracavity optical elements as before.

Figure 12 displays the dynamic response of the cavity eigenmodes as a function of rod focal length.

In Figure 12 it is evident that the focusing characteristics of the pumping field in the Raman medium is largely dependent of the input power. Dynamic focusing will therefore affect both the Raman conversion efficiency and the cavity mode-matching.

Geometry can play a significant role in mitigating thermal induced lensing and stress birefringence in gain medium. It is well known that stress induced biaxial focus, depolarization (as a result of stress induced birefringence) and first order thermal focusing is eliminated in the zig-zag slab geometry (see Figure 2)⁶. Only second order thermally induced distortion will be left as a lensing effect. As a

result of the geometry, this lensing will add a cylindrical component to the phase front. Because the beams enter and exit the slab at Brewster's angle, this component will add an astigmatism which is partially canceled by the Brewster medium. Hence, thermally induced distortion lensing is a small effect and slab geometries for both the laser and Raman medium should be implemented in high average power Raman laser designs.

In laser and Raman media, thermal distributions result from absorption of pumping radiation due to a non-zero quantum defect. The quantum defect can be minimized by directly pumping low lying pumping manifolds with high-power single frequency sources such as laser diodes. As with laser media, Raman medium will also heat significantly (if Stokes radiation is oscillating) due to the finite quantum defect between the pumping radiation and the first Stokes radiation. In solid-state Raman medium the quantum defect is on the order of 1000 cm^{-1} as opposed to $\sim 3400\text{ cm}^{-1}$ in gaseous media. Therefore less heat is deposited per photon in solid-state Raman medium.

4.4. Cavity Mode Build-up Dynamics

Power-oscillators are attractive because they can provide high-average-power optical radiation at a fraction of the cost of an equivalent master oscillator power amplifier (MOPA). Modeling cavity mode build-up dynamics can be a very valuable tool in the design of power-oscillators. Two main effects surface in the model: (1) itinerant foci, and (2) diffraction loss.

When the cavity modes builds up from noise the amplified radiation can be focused in locations not predicted by the eigenmode solution of the cavity. This

is because the eigenmode is achieved only in the steady state, i.e. after several tens of roundtrips. When the transient behavior of the mode build up is examined, itinerant foci can be observed. If these itinerant foci coincide with intracavity optical elements damage can ensue.

Equally as important in the design of power-oscillators are the effects of diffraction losses for higher order modes. In the case of efficient, near diffraction limited, high-power Raman lasers it is advantageous to design the pumping power-oscillator to operate in a high order multimode for low repetition rate high-average-power Raman lasers (30 to 300 Hz), and low order multimode for high repetition rate high-average-power Raman lasers (1 to 10 kHz).

The mode evolution of intracavity Raman lasers can be approximated using the first-order multimode design techniques previously discussed. However, the techniques are only strictly valid in the steady-state because the Raman gain is strongly dependent on the transient pumping field amplitude and distribution. What matters in an intracavity Raman laser is the mode structure when Raman threshold is achieved, not in steady-state.

The diffraction propagation code described earlier can be used to model the cavity buildup dynamics. Figure 13 shows an example of the transient cavity mode buildup when the cavity is seeded with a noisy high order field distribution.

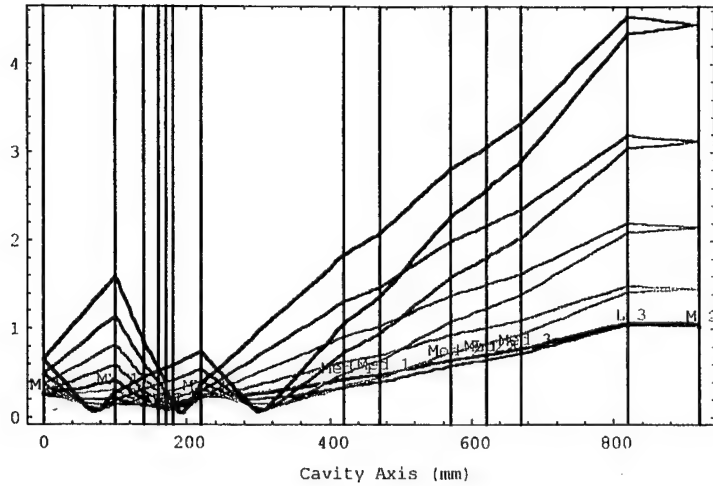


Figure 13: Transient sagittal mode evolution of the example Raman laser described by Figure 5. Five passes of the pump laser resonator are shown. The first pass is red and the last blue. Note the formation of itinerate foci at ~ 75 mm and ~ 300 mm long the cavity axis. Transverse mode control can be implemented to reduce itinerate foci.

4.5. *Intracavity Raman Beam Cleanup*

The mechanism for Raman beam cleanup is most easily understood by examining the driving polarizations responsible for SRS, given by⁷

$$\mathcal{P}_P(r_\perp, z) = \bar{\chi}_{R_P}^{(3)} \cdot |\mathcal{E}_S(r_\perp, z)|^2 \mathcal{E}_P(r_\perp, z) \quad (5.1)$$

and

$$\mathcal{P}_S(r_{\perp}, z) = \bar{\chi}_{R_S}^{(3)} \cdot |\mathcal{E}_P(r_{\perp}, z)|^2 \mathcal{E}_S(r_{\perp}, z) \quad (5.2)$$

It should be noted that the relative phase of the Stokes field canceled in Eq. 5.1 and that of the pump in Eq. 5.2. This has lead researchers in the past to refer to the Raman conversion process as a "phase-matchless" process. By taking a more careful look at these terms we will show this to be a misconception. It is true, however, that by virtue of this apparent cancellation the stimulating fields in Eqs. 5.1 and 5.2 see only the intensity of the Stokes and pump fields, respectively. This fact, in and of itself, sets the Raman conversion process apart from other common phase-matched three and four wave interactions, such as SHG, OPO and FWM.

Applying the convolution theorem⁸ to Eqs. 5.1 and 5.2 we find that, in terms of the pump and Stokes spectrums,

$$\mathcal{P}_P(r_{\perp}, z) = \bar{\chi}_{R_P}^{(3)} \cdot \int dk \mathcal{E}_S(k, z) \ast \ast \mathcal{E}_S(k, z) \ast \ast \mathcal{E}_P(k, z) e^{-ik \bullet r} \quad (5.3)$$

$$\text{and } \mathcal{P}_S(r_{\perp}, z) = \bar{\chi}_{R_S}^{(3)} \cdot \int dk \mathcal{E}_P(k, z) \ast \ast \mathcal{E}_P(k, z) \ast \ast \mathcal{E}_S(k, z) e^{-ik \bullet r} \quad (5.4)$$

where \mathbf{k} is the wave vector ($\mathbf{k} = 2\pi \mathbf{p}_{\perp}$) and $\ast \ast$ represents the two dimensional convolution operation. In generating the stimulated Stokes field it is evident, therefore, that each plane wave component of the pump field mixes with every other pump component via the complex autocorrelation $\gamma_P(\mathbf{k}) = \mathcal{E}_P(\mathbf{k}, z) \ast \ast$

$\mathcal{E}_p(\mathbf{k}, z)$. This apparent pump spectrum is then combined with all possible plane wave components of the seeding Stokes field, via the convolution $\gamma_p(\mathbf{k}) \ast \mathcal{E}_s(\mathbf{k}, z)$. Therefore, if the pump and Stokes spectrum are sufficiently well behaved functions (a condition that is almost always obeyed in paraxial optics), then the stimulated Stokes field will be a smoothed version of the seeding Stokes spectrum. This smoothing operation is performed twice per round trip in the Raman laser resonator. The Central Limit Theorem⁸ predicts a Gaussian spectrum to result from a multi-order spectral convolution, where the order is greater than three. Therefore, a Gaussian transverse field distribution can ensue after only a few round trips of the laser cavity. Under the conditions of adequate single pass Raman gain and cavity mode matching a $TEM\infty$ diffraction limited Raman laser output can be achieved over a very large dynamic range, without the use of intracavity apertures.

4.5.1. Computer Modeling of Intracavity Raman Beam Cleanup.

As an initial example of intracavity Raman beam cleanup, a simple traveling wave ring oscillator containing only a Raman medium was modeled with *Lasica*. In this way only Raman conversion and diffraction contribute the shape of the transverse field distributions, i.e. spatial filtering of intracavity apertures and gain saturation effects do not obscure the results. This simple cavity is shown schematically in Figure 14 below.

In this example, we chose "top-hat" field distributions as seeding pump and Stokes fields to approximate a high-order, multimode beam profile, as shown in Figure 15 (a). Figure 15 (b) displays the pump and Stokes field after taking three full roundtrips of the cavity. Here we note that the Stokes field is nearly a perfect Gaussian distribution and the pump field distribution is similar to the expectant $\text{sinc}^2\chi$ far-field (Fraunhofer) diffraction pattern resulting from a

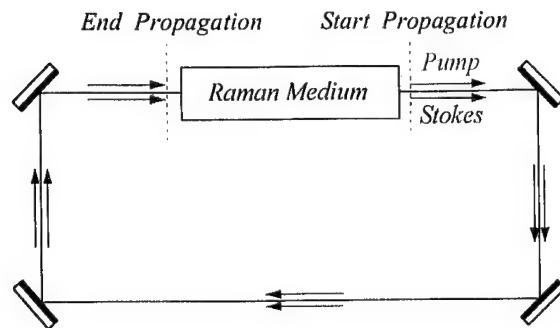


Figure 14: Example traveling wave resonator used to demonstrate intracavity Raman beam cleanup. Seeding pump and Stokes beams are injected just after the Raman medium and propagated around the ring to a plane just before the Raman medium. Gain-propagation steps are then taken through the Raman medium. This Procedure is executed several times.

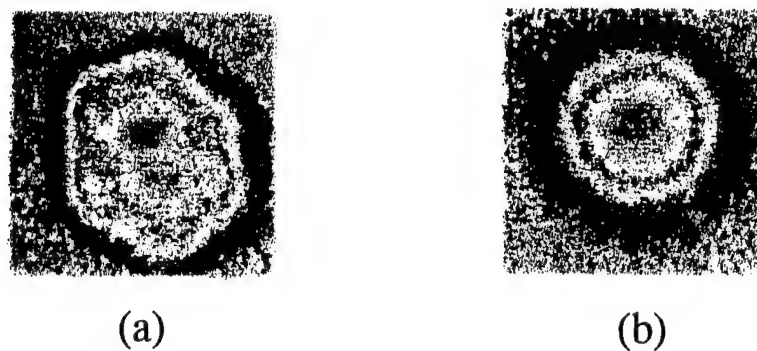


Figure 15: Intracavity beam cleanup. (a) Multi-mode pump beam profile ($1.338 \mu\text{m}$), and (b) single mode, diffraction limited Stokes beam profile ($1.556 \mu\text{m}$).

rectangular (top-hat) initial distribution⁸, only the distribution show noticeable signs of depletion.

This theory is well supported by our experimental results. Figure 16 shows the intracavity pump and first Stokes beam profiles obtained from a $1.556\text{ }\mu\text{m}$ Raman laser built in our laboratory. It is evident that the highly multimode pump field has been "converted" into a near diffraction limited Stokes output beam. No transverse mode control was implemented in either the pump or Raman cavity.

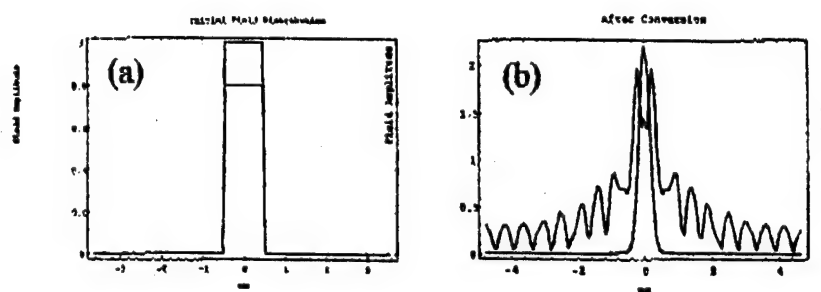


Figure 16: Pump (blue) and first Stokes (red) transverse field distributions: (a) Seeded pump and Stokes fields, and (b) pump and Stokes fields after three roundtrips of the cavity.

4.6. Resonator Dynamics

Intracavity solid state Raman scattering has been modeled using rate equations and specific laser parameters to predict actual device characteristics. Pulse dynamics, energy output per pulse and average power output for a given pumping scheme and laser host, overall efficiency, and the intensity levels in the

Raman crystal for conversion optimization are of interest in a specific application.

For the 25 mJ per pulse 100 Hz rep rate system the overall efficiency depends on the specific diode pumped slab design. Optimization requires compromises between cost, efficiency, complexity and reliability, stability, and survivability. The approach for this transmitter uses direct diode side pumping in a configuration that produces a uniform pump intensity throughout the zig-zag slab.

Beam cleanup and conversion efficiency require coupled Raman and pump resonators. This model uses coupled cavity rate equations to define design values for the optical elements and to optimize performance. We input the results of the resonator model to the rate equations to calculate the performance characteristics.

4.7. Pump Characteristics.

Analysis starts with laser diode pump power estimated from diode specifications, and the pump power converted to population inversion within the laser resonator mode volume in the slab. This value is used to calculate the threshold and the initial and final population inversion densities for the correct cavity losses from the intracavity elements. These values can be used to estimate the pulse energy and average power output for a given rep rate at the pump wavelength, and to calculate the initial conditions for the rate equations.

4.8. Raman Characteristics.

The Raman cavity is characterized using the steady state Raman gain coefficient and the stimulated Stokes cross section for the Raman material. Raman cavity losses for the intracavity elements are estimated for use in the rate equations. Additional effects are included in the rate equations for finite Q-switch switching time and second Stokes wavelength generation. Figure 17 shows the output pulse characteristics for the inversion density, pump pulse at $1.338 \mu\text{m}$, and Raman pulse at $1.56 \mu\text{m}$.

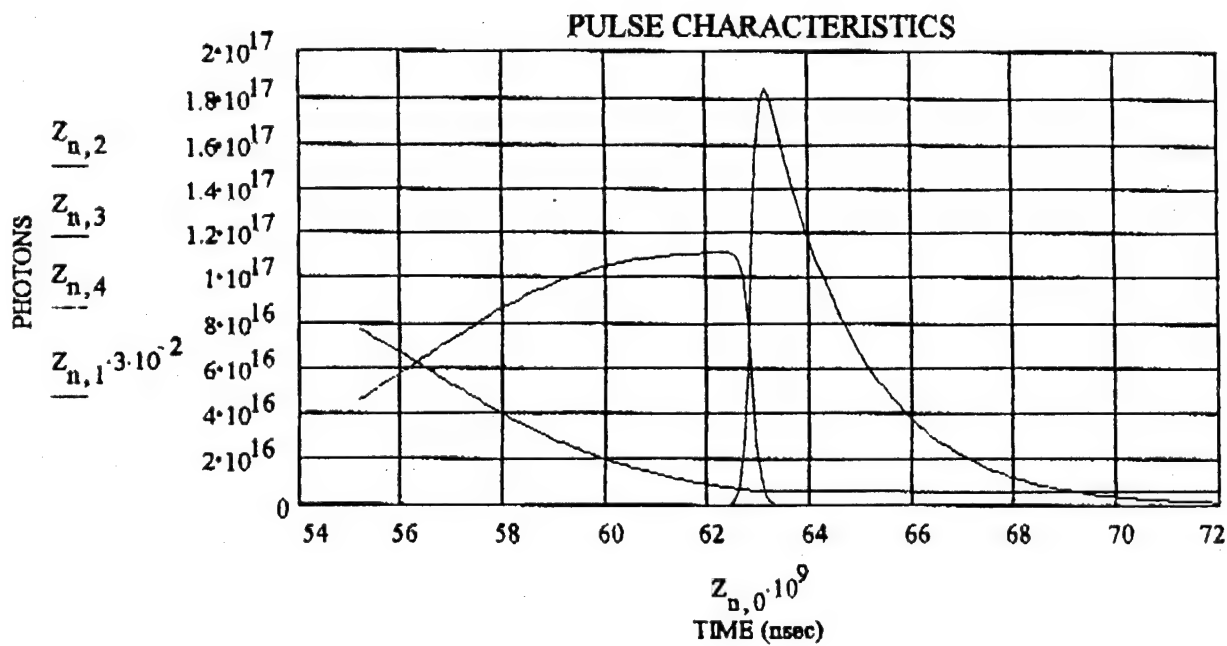


Figure 17: Pulse characteristics for 2.5 watt average power diode pumped slab. The black curve is the population inversion stored in the slab, the red curve is the pump pulse at $1.338 \mu\text{m}$ and the blue curve is the Raman output pulse. The FWHM of the pump pulse is $\tau_p \sim 7 \text{ nsec}$ and the FWHM of the Raman pulse is $\tau_R \sim 1.7 \text{ nsec}$.

The Raman cavity optimum output coupling, maximum peak power and energy per pulse level and average power output can be estimated from the Raman output pulselwidth and the Rigrod analysis using the gain and losses in the Raman cavity and the saturation intensity for the Raman crystal. The output energy per pulse and average power output are estimated from the results of the Rigrod analysis. Figure 18 shows the calculation results for the Raman output coupling.

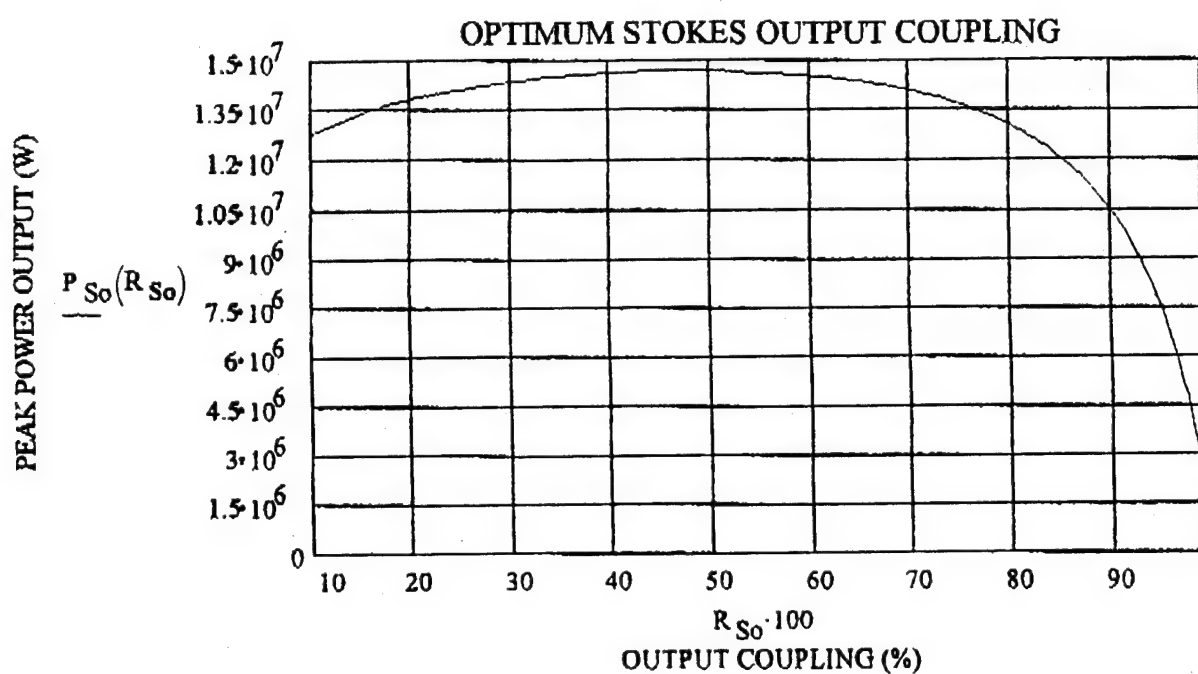


Figure 18: Raman cavity output coupling and peak power levels. Optimum output coupling for this configuration is a reflectivity of 48%.

To achieve 2.5 watts of average power output a 50 watt QCW laser diode will be used to pump the zig-zag slab. Based on the 50 watt QCW diode input power the Raman energy per pulse at 1.56 um calculated from the peak power at optimum outcoupling in the Rigrod analysis is $E = (P_{pk})(\tau_R) = 25$ mJ/pulse, for a

pulsewidth of 1.7 nsec, calculated from the rate equations. The average power at 100 Hz rep rate is $P_{ave} = (E)(f) = 2.5$ watts.

5. COMMERCIAL ANALYSIS

Events that have occurred during the past several years including episodes in the Gulf War and terrorist attacks in the Tokyo subway have vividly demonstrated the seriousness of chemical and biological attacks. Therefore, it is vitally important that this country have high technology systems for rapidly detecting and identifying chemical and biological aerosols at long range. Laser standoff chemical and biological detection systems based on lidar schemes appear to be the best technology for this application. So far the ideal laser transmitter for these systems has not been developed.

Remote sensing lidar systems can be used to detect chemical and biological aerosols through several mechanisms including differential absorption, laser-induced fluorescence, and back scattered laser light. Each different type of lidar system requires a laser transmitter with specific operating characteristics in terms of output wavelength, temporal pulse length, spectral pulse width and stability. To achieve the significant advance in solid state laser technology required to develop a variety of laser sources optimized for these specific operating characteristics, an innovative approach to laser systems design is needed. The unique intracavity Raman laser concept proposed here provides that innovative approach. In addition, the computer modeling code for coupled cavity, nonlinear optical systems employed here is ideal for designing tailor-made lasers optimized for specific operating characteristics.

The laser system developed in this research project will have the operating characteristics that make it an ideal transmitter for a lidar system at 1.56 μm . In

addition, it will have the operating characteristics that make it ideal as a pump laser for an OPO that results in tunable radiation in the near to mid-IR spectral region, or for frequency doubling, tripling, and quadrupling crystals that result in coherent emission in the visible and near UV spectral regions. Thus the coherent radiation source resulting from this project will be useful in laser radar and imaging systems operating in any spectral region from the near UV to the mid-IR. The primary laser emission at $1.56 \mu\text{m}$ is of specific interest because this wavelength provides eye-safe operation in a spectral window with maximum transmission in the atmosphere. Because this will be an all solid state laser, it will be a rugged, lightweight, and robust system. Environmental stability and reduced maintenance requirements will improve reliability in the field.

The system developed during this project will have commercial applications for any area requiring high power, tunable, coherent radiation. The infrared system to be developed as a prototype can be converted to operation in the visible or near ultraviolet spectral regions by appropriate selection of nonlinear optical crystals and the pump laser. Two specific areas where high power tunable coherent sources are needed are missile counter measures, and lidar systems used for detection and imaging of atmospheric pollutants and wind shear as well as for aircraft collision avoidance systems.

This diffraction limited source is intended to be used in pumping high average power optical parametric amplifiers tunable from the UV to the mid IR. This wavelength solves the pump absorption problem with $1 \mu\text{m}$ sources in some nonlinear crystals used in OPO devices, and moves the idler to a more desirable wavelength. Tunable source applications include military IR countermeasures and chem/bio sensors to improve discrimination through multispectral imaging. Medical applications include dermatology (removal of port wine stains, tattoos,

skin cancer, moles, etc.) where precise wavelength for absorption is critical to procedure effectiveness. A degenerate OPO pumped by this source would generate output at 3 μm in a pulse format from single shot to greater than 10 kHz rep rate. Such a system would have application in the medical market for cutting both hard and soft tissue. Commercial applications for a tunable source include remote sensing monitoring of pollutants, entertainment in light shows and a dazzler for law enforcement.

Through the requirements generated by the general and specific applications listed above, it is obvious that there is a significant market potential for commercial solid state laser systems.

6. RESULTS AND CONCLUSIONS

We have demonstrated a solid-state Raman laser using a Brewster cut, Ba(NO₃)₂ crystal. The Ba(NO₃)₂ crystal was placed within a high finesse (~1600), Q-switched, Nd:YAG laser cavity which operated simultaneously at 1.319 and 1.338 μm . The gain for the nitrate moiety ν_1 (A₁') breathing mode at 1047 cm⁻¹ that dominates all other Raman active modes produced simultaneous output at 1.535 and 1.556 μm . Single pump line and concomitantly, single Raman line can be achieved by the addition of a frequency selective intracavity element in the laser resonator.

The Optical layout of the Raman laser resonator is shown in Figure 19. The Raman laser consists of two standing wave resonators coupled by a dielectric beamsplitter. Two high reflecting mirrors (HR) define the "L" shaped 1.3 μm laser cavity. The 1.5 μm Raman cavity is defined by the HR and 50% reflective output coupler (OC) (dual lines show the shared portion of the cavity). An "ABCD" calculation was performed to calculate the relative mirror separations to mode-match the two cavities.

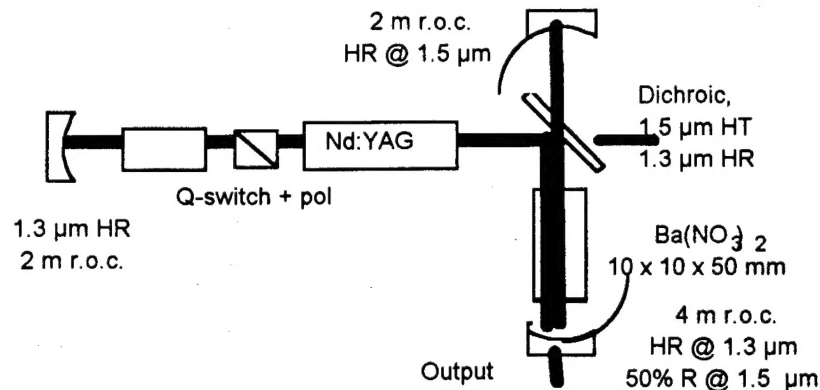
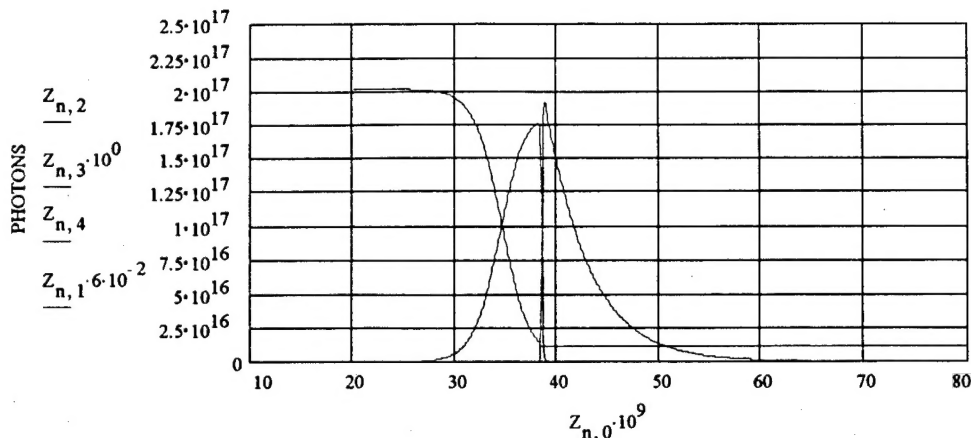
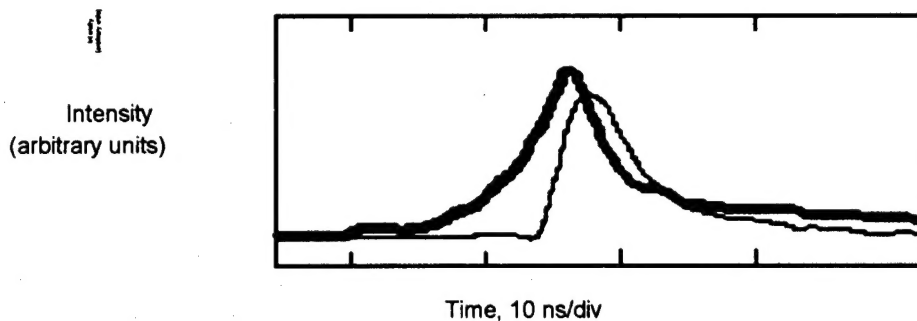


Figure 19: Optical layout of the intracavity SSRS and pump laser. The physical length of the laser cavity is 69 cm and the Raman cavity is 40 cm long. The configuration matches the mode waists of the two cavities, accounting for the wavelength dependent change in diffraction limited spot sizes and media-induced optical path differences

Figure 20 show the temporal profiles of the pump and Stokes emissions. The 1.3 μm temporal profile was measured by monitoring intracavity light transmitted through the 45° dielectric beamsplitter using a monochromator and Ge photodiode. Similarly, the temporal behavior of the Stokes emission was measured from light transmitted out the Raman resonator's HR mirror. A dielectric filter which rejects the 1.3 μm pump light and transmits the 1.5 μm Raman output was placed in front of a separate Ge photodiode which detected the Raman emission. The deconvolved 1.5 μm pulse width is on the order 6 ns. The Raman gain was low enough that self-modelocking was not induced by gain-switching. A theoretical model was developed that agrees well with the temporal and energy extraction data. This model can be used to determine cavity and crystal parameters for tailored output pulse-widths.



(a)



(b)

Figure 20: (a) Modeling of the pump depletion and Raman emission. The maximum 1.3 μm output of the Nd:YAG laser without the Raman conversion would correspond to 25 mJ/pulse. The slower risetime curve is the 1.3 μm pump pulse and the delayed, rapidly rising pulse is the first Stokes output at 1.5 μm . The result shows the well defined Raman threshold, pump depletion and high Raman gain. (b) oscilloscope trace of the temporal profile of pump and Raman emission. Pump is dark solid line and Raman output is thin solid line.

The optical-to-optical conversion efficiency was estimated to be ~60% by taking the ratio of the Stokes output energy to the pump energy with the pump output optimized. The optimized pump output energy was measured with the $\text{Ba}(\text{NO}_3)_2$ crystal in the cavity, but with the Raman arm blocked and near-optimal 1.3 μm output coupler ($R \sim 40\%$) in place of the Raman output coupler. Saturation of the

Raman gain was not observed at the power levels probed thus far. Higher efficiencies are anticipated for higher pump pulse energies. The quality of the Pockels cell used to Q-switch the laser limited our measurements to 250 mJ of 1.5 μm . The ultimate conversion efficiency is quantum limited to 86 % for the 1.338 - 1.556 μm Raman shift. Optimized Stokes output can be achieved by carefully selecting cavity beam parameters and crystal lengths to vary the Raman gain.

We believe the laser system described here has delivered the highest brightness, best quality, high energy 1.56 μm pulses to date and anticipate high average powers (50 to 100 W) in the near term. This method is extremely efficient and simplistic. The elegance and simplicity of this method lends itself to robust, portable, fieldable, high power, eye-safe, active remote sensing systems. In addition, other materials are being investigated to establish their potential for application as Raman laser sources.

DISTRIBUTION LIST

AUL/LSE
Bldg 1405 - 600 Chennault Circle
Maxwell AFB, AL 36112-6424 1 cy

DTIC/OCP
8527 John J. Kingman Rd, Suite 0944
Ft Belvoir, VA 22060-6218 2 cys

AFSAA/SAI
1580 Air Force Pentagon
Washington, DC 20330-1580 1 cy

PL/SUL
Kirtland AFB, NM 87117-5776 2 cys

PL/HO
Kirtland AFB, NM 87117-5776 1 cy

Official Record Copy
PL/LIDA
Kirtland AFB, NM 87117-5776
Attn: Maj Peter S. Durkin 2 cys